A second-order accurate in time IMplicit-EXplicit (IMEX) integration scheme for sea ice dynamics

Jean-François Lemieux[a,*], Dana A. Knoll[b], Martin Losch[c], Claude Girard[d]

[a] *Recherche en Prévision Numérique environnementale/Environnement Canada, 2121 route Transcanadienne, Dorval, Qc H9P 1J3, Canada*
[b] *Los Alamos National Laboratory, P.O. Box 1663, Los Alamos, NM 87545, USA*
[c] *Alfred-Wegener-Institut, Helmholtz-Zentrum für Polar-und Meeresforschung, Postfach 120161, 27515, Germany*
[d] *Recherche en Prévision Numérique atmosphérique/Environnement Canada, 2121 route Transcanadienne, Dorval, Qc H9P 1J3, Canada*

Abstract

Current sea ice models use numerical schemes based on a splitting in time between the momentum and continuity equations. Because the ice strength is explicit when solving the momentum equation, this can create unrealistic ice stress gradients when using a large time step. As a consequence, noise develops in the numerical solution and these models can even become numerically unstable at high resolution. To resolve this issue, we have implemented an iterated IMplicit-EXplicit (IMEX) time integration method. This IMEX method was developed in the framework of an already implemented Jacobian-free Newton-Krylov solver. The basic idea of this IMEX approach is to move the explicit calculation of the sea ice thickness and concentration inside the Newton loop such that these tracers evolve during the implicit integration. To obtain second-order accuracy in time, we have also modified the explicit time integration to a second-order Runge-Kutta approach and by introducing a second-order backward difference method for the implicit integration of the momentum equation. These modifications to the code are minor and straightforward. By comparing results with a reference solution obtained with a very small time step, it is shown that the approximate solution is second-order accurate in time. The new method permits to obtain the same accuracy as the splitting in time but by using a time step that is 10 times larger. Results show that the second-order scheme is more than five times more computationally efficient than the splitting in time approach for an equivalent level of error.

*Corresponding author
Email address: jean-francois.lemieux@ec.gc.ca (Jean-François Lemieux)

Keywords: sea ice, IMEX method, backward difference, Newton-Krylov method, numerical accuracy

1. Introduction

Various mechanisms associated with sea ice dynamics play a key role in shaping the ice cover of the polar oceans. To properly model the processes of lead and pressure ridge formation, sea ice models require a sophisticated representation of sea ice rheology, i.e. the relation between internal stresses, material properties (ice strength) and deformations of the ice cover. Most current sea ice models use the Viscous-Plastic (VP) formulation of Hibler [1] to represent these ice interactions. The VP formulation leads to a very nonlinear problem which is known to be difficult to solve.

To the best of our knowledge, all sea ice model time integration schemes are based on a splitting in time between the momentum and the continuity equations (e.g., [1, 2, 3, 4, 5]). This means that when solving the momentum equation, the thickness distribution (including the amount of open water) is held constant at the previous time level (it, however, varies spatially). Once the velocity field is obtained, the thickness distribution is advanced to the next time level. Furthermore, an operator splitting approach is generally used to separate the change of the thickness distribution associated with advection and the growth/melt related to thermodynamic processes (e.g., [2, 3]). This paper focuses on dynamics and we therefore only discuss the solution of the momentum equation and of the continuity equation without the thermodynamic source terms.

Current sea ice model numerical schemes suffer from significant numerical issues. First, as explained by Lipscomb et al. [2], the splitting in time approach leads to noise in the numerical solution and can even make the model numerically unstable. As an illustrative example, consider ice converging toward a coast due to an onshore wind; a stress gradient, associated with an ice strength gradient, develops to oppose the wind stress. When using a large time step with the splitting in time approach, an unrealistically large ice strength gradient can occur. The stress gradient force can then overcompensate the wind stress and cause an unrealistic reversal of the flow (the ice then diverges at the coast). This instability, fundamentally numerical, can be cured by reducing the time step. Unfortunately, this obviously increases the total computational time. Lipscomb et al. [2] proposed a modification to the ridging scheme in order to mitigate this problem.

A second numerical issue is related to the solution of the momentum equation. The rheology term, which determines the deformations of the ice cover based on the internal ice stresses, causes the momentum equation to be very nonlinear. Indeed, the VP rheology leads to a large change in the internal stresses when going from a slightly convergent flow to a slightly divergent one (same idea for shear stresses). The current numerical solvers for the momentum equation, however, have difficulties in finding the solution of this very nonlinear problem. There are two main classes of schemes to solve the momentum equation: the implicit solvers, which involve an outer loop iteration (sometimes referred to as Picard iteration, [5, 6, 7]) and the ones based on the explicit solution of the momentum equation using the Elastic-VP approach [8, 9]. Both of these approaches, however, lead to a very slow convergence rate [7, 9] if they converge at all [9, 10]. Because of this slow convergence rate, it is typical to perform a small number of Picard iterations or of subcycling iterations. The approximate solution therefore contains residual errors which are carried on in the time integration.

To resolve this slow convergence rate issue, Lemieux et al. [4] developed a Jacobian-free Newton-Krylov (JFNK) implicit solver. They showed that the JFNK solver leads to a more accurate solution than the EVP solver [10] and that it is significantly more computationally efficient than a Picard approach [4]. Following the work of Lemieux et al. [4], Losch et al. [11] have recently developed a parallel JFNK solver for the MIT general circulation model with sea ice [12]. The numerical approaches of Lemieux et al. [4] and Losch et al. [11], however, still rely on the splitting in time scheme and are therefore susceptible to exhibit the numerical instability issue.

It is the purpose of this paper to introduce a fast and accurate time integration scheme that resolves the instability associated with the splitting in time approach. One possibility would be to solve fully implicitly the momentum and continuity equations. This avenue would imply significant modifications to the code and would be quite complex to implement. Instead, the splitting in time issue is cured by using an iterated IMplicit-EXplicit

(IMEX) approach when solving the momentum and continuity equations. This approach is built around our existing JFNK solver. Basically, the idea is to move the explicit calculation of the thickness distribution inside the implicit Newton loop. We take this approach one step further by modifying the time integration in order to get second-order accuracy in time for the full system. To do so, we introduce a second-order Runge-Kutta scheme for the advection operation and discretize in time the momentum equation using a second-order backward difference (as in [13]). This paper is inspired by the work of [14, 15] on an iterated IMEX method for radiation hydrodynamics problems.

The main contribution of this paper is the development and demonstration of a first-of-a-kind second-order accurate in time iterated IMEX integration scheme for sea ice dynamics. This manuscript also shows the gain in accuracy and computational time of the second-order IMEX method compared to the common first-order integration scheme based on the splitting in time.

It is worth mentioning that some authors have recently questioned the validity of the VP rheology. Sea ice models based on a VP rheology do not capture the largest deformations events [16] and statistics of simulated deformations do no match observations [16] in both space and time [17]. While some authors propose new and very different formulations of ice interactions [18, 19], others claim that a VP rheology with modified yield curve and flow rule can adequately represent the sea ice deformations [20]. These new physical parameterizations, under evaluation, also lead to very nonlinear problems which would also clearly benefit from the availability of reliable and efficient numerical schemes.

This paper is structured as follows. Section 2 describes the sea ice momentum equation with a VP formulation and the continuity equation. In section 3, the discretization of the momentum and continuity equations and the descriptions of the standard splitting in time and new IMEX integration schemes are presented. In section 4, more information about the model is given. The description of the experiments and the results are outlined in section 5. A discussion and concluding remarks are provided in section 6.

2. Sea ice momentum and continuity equations

As the ratio between the horizontal and the vertical scales is O(1000 km/10 m) = O(10^5), sea ice dynamics is often considered to be a two-dimensional problem [21]. The two-dimensional sea ice momentum equation is obtained by integrating in the vertical the momentum equation. It is given by

$$\rho h \frac{D\mathbf{u}_2}{Dt} = -\rho h f \mathbf{k} \times \mathbf{u}_2 + \tau_a - \tau_w + \nabla \cdot \sigma - \rho h g \nabla H_d, \quad (1)$$

where ρ is the density of the ice, h is the ice volume per unit area (or the mean thickness and just referred to as thickness in this paper), $\frac{D}{Dt}$ is the total derivative, f the Coriolis parameter, $\mathbf{u}_2 = u\mathbf{i} + v\mathbf{j}$ the horizontal sea ice velocity vector, $\mathbf{i}$, $\mathbf{j}$ and $\mathbf{k}$ are unit vectors aligned with the x, y and z axis of our Cartesian coordinates, τ_a is the wind stress, τ_w the water stress, σ the internal ice stress tensor ($\nabla \cdot \sigma$ is defined as the rheology term), g the gravity and H_d the sea surface height. The subscript in $\mathbf{u}_2$ indicates that it is a 2-D vector and it is used to distinguish $\mathbf{u}_2$ from the vector $\mathbf{u}$ obtained from the spatial discretization (explained in section 3).

As in Tremblay and Mysak [3], the sea surface tilt is expressed in terms of the geostrophic ocean current. Using a quadratic law and constant turning angles θ_a and θ_w, τ_a and τ_w are expressed as [22]

$$\tau_{\mathbf{a}} = \rho_a C_{da} |\mathbf{u}_a^g| (\mathbf{u}_a^g \cos\theta_a + \mathbf{k} \times \mathbf{u}_a^g \sin\theta_a), \quad (2)$$

$$\tau_{\mathbf{w}} = \rho_w C_{dw} |\mathbf{u}_2 - \mathbf{u}_w^g| [(\mathbf{u}_2 - \mathbf{u}_w^g) \cos\theta_w + \mathbf{k} \times (\mathbf{u}_2 - \mathbf{u}_w^g) \sin\theta_w], \quad (3)$$

where ρ_a and ρ_w are the air and water densities, C_{da} and C_{dw} are the air and water drag coefficients, and $\mathbf{u}_a^g$ and $\mathbf{u}_w^g$ are the geostrophic wind and ocean current. As $\mathbf{u}_2$ is much smaller than $\mathbf{u}_a^g$, it is neglected in the expression for the wind stress.

The VP constitutive law, that relates the internal stresses and the strain rates, can be written as [1]

$$\sigma_{ij} = 2\eta\dot{\epsilon}_{ij} + [\zeta - \eta]\dot{\epsilon}_{kk}\delta_{ij} - P\delta_{ij}/2, \quad i,j = 1,2, \quad (4)$$

where σ_{ij} are the components of the ice stress tensor, δ_{ij} is the Kronecker delta, $\dot{\epsilon}_{ij}$ are the strain rates defined by $\dot{\epsilon}_{11} = \frac{\partial u}{\partial x}$, $\dot{\epsilon}_{22} = \frac{\partial v}{\partial y}$ and $\dot{\epsilon}_{12} = \frac{1}{2}(\frac{\partial u}{\partial y} + \frac{\partial v}{\partial x})$, $\dot{\epsilon}_{kk} = \dot{\epsilon}_{11} + \dot{\epsilon}_{22}$, ζ is the bulk viscosity, η is the shear viscosity and P is a pressure-like term which is a function of the ice strength.

With a two-thickness category model, the ice strength P_p is parameterized as

$$P_p = P^* h \exp[-C(1-A)], \tag{5}$$

where P^* is the ice strength parameter, A is the sea ice concentration and C is the ice concentration parameter, an empirical constant characterizing the strong dependence of the compressive strength on sea ice concentration [1].

The formulation of the bulk and shear viscosities depends on the yield curve and the flow rule. In the following, the elliptical yield curve with a normal flow rule [1] is used. In this case, the bulk and shear viscosities are given by

$$\zeta = \frac{P_p}{2\triangle}, \tag{6}$$

$$\eta = \zeta e^{-2}, \tag{7}$$

where $\triangle = [(\dot{\epsilon}_{11}^2 + \dot{\epsilon}_{22}^2)(1+e^{-2}) + 4e^{-2}\dot{\epsilon}_{12}^2 + 2\dot{\epsilon}_{11}\dot{\epsilon}_{22}(1-e^{-2})]^{\frac{1}{2}}$, and e is the aspect ratio of the ellipse, i.e. the ratio of the long and short axes of the elliptical yield curve.

When $\triangle$ tends toward zero, equations (6) and (7) become singular. To avoid this problem, ζ is capped using an hyperbolic tangent [7]

$$\zeta = \zeta_{max} \tanh(\frac{P_p}{2\triangle\zeta_{max}}). \tag{8}$$

As in equation (7), $\eta = \zeta e^{-2}$. The coefficient ζ_{max} is set to the value proposed by Hibler [1]: $2.5 \times 10^8 P_p$ (this is equivalent to limiting $\triangle$ to a minimum value of $2 \times 10^{-9}\mathrm{s}^{-1}$). As opposed to the regularization introduced by Hibler [1], this formulation for ζ is continuously differentiable.

We use a replacement closure similar to the one presented in Kreyscher et al. [23]. The pressure term is given by

$$P = 2\zeta\triangle. \tag{9}$$

The continuity equations for the thickness and the concentration are given by

$$\frac{\partial h}{\partial t} + \nabla\cdot(\mathbf{u}_2 h) = S_h, \tag{10}$$

$$\frac{\partial A}{\partial t} + \nabla\cdot(\mathbf{u}_2 A) = S_A, \tag{11}$$

where S_h and S_A are thermodynamic source terms. Note that A is limited above to 1.0. This does not affect the conservation of mass as the mass per m^2 is given by ρh. The source terms in equations (10) and (11) are set to zero in the simulations for this paper (unless otherwise stated) as we concentrate on matters related to the dynamics.

3. Numerical approaches

3.1. Temporal discretization

The advection of momentum is neglected as it is small compared to the other terms in the momentum equation (as done in [6, 8]). The momentum and continuity equations are solved at time levels Δt, $2\Delta t$, $3\Delta t, \ldots$ where Δt is the time step and the index $n = 1, 2, 3, \ldots$ refers to these time levels.

The standard numerical approach involves a Splitting In Time (SIT) between the implicit momentum and explicit continuity equations. This splitting implies that h and A (and therefore P_p) are considered to be known in the momentum equation as they are held at the previous time level. Using a backward Euler approach for the acceleration term, the u and v momentum equations at time level n are written as

$$\rho h^{n-1}\frac{(u^n - u^{n-1})}{\Delta t} = \rho h^{n-1} f v^n + \tau_{au}^n - \tau_{wu}^n + \frac{\partial \sigma_{11(P_p^{n-1})}^n}{\partial x} + \frac{\partial \sigma_{12(P_p^{n-1})}^n}{\partial y}, \tag{12}$$

$$\rho h^{n-1}\frac{(v^n - v^{n-1})}{\Delta t} = -\rho h^{n-1} f u^n + \tau_{av}^n - \tau_{wv}^n + \frac{\partial \sigma^n_{22(P_p^{n-1})}}{\partial y} + \frac{\partial \sigma^n_{12(P_p^{n-1})}}{\partial x}, \quad (13)$$

where the sea surface tilt term is ignored here to simplify the presentation. As the water drag and the rheology term are written in terms of the velocity field, the only unknowns in equations (12) and (13) are u^n and v^n. Once these equations are solved for u^n and v^n everywhere on the grid, the thickness and concentration fields are advanced in time according to

$$\frac{(h^n - h^{n-1})}{\Delta t} + \nabla \cdot (\mathbf{u}_2^n h^{n-1}) = 0, \quad (14)$$

$$\frac{(A^n - A^{n-1})}{\Delta t} + \nabla \cdot (\mathbf{u}_2^n A^{n-1}) = 0, \quad (15)$$

for which we use a first-order (in space) upstream scheme (as in [3, 23, 24]). We introduce the operator L given by

$$h^n = L(h^{n-1}, \mathbf{u}_2^n), \quad (16)$$

which allows one to write concisely the explicit calculation of h^n based on the upstream scheme (same idea for A^n). This scheme is stable if the Courant-Friedrichs-Lewy (CFL) condition $\max(u, v) < \frac{\Delta x}{\Delta t}$ is respected, with Δx being the spatial resolution.

This scheme for the integration of the momentum and continuity equations is first-order accurate in time as a consequence of the first-order treatment in both the momentum and continuity equations, and as a result of the SIT splitting error which is not iterated. We here introduce a few straightforward modifications that allows one to solve simultaneously these equations with second-order accuracy in time.

First, we introduce a second-order backward difference (BDF2, [13]) approach for the momentum equation. Hence, the u and v equations are written as

$$\frac{\rho h^n}{\Delta t}\left(\frac{3}{2}u^n - 2u^{n-1} + \frac{1}{2}u^{n-2}\right) = \rho h^n f v^n + \tau_{au}^n - \tau_{wu}^n + \frac{\partial \sigma^n_{11(P_p^n)}}{\partial x} + \frac{\partial \sigma^n_{12(P_p^n)}}{\partial y}, \quad (17)$$

$$\frac{\rho h^n}{\Delta t}(\frac{3}{2}v^n - 2v^{n-1} + \frac{1}{2}v^{n-2}) = -\rho h^n f u^n + \tau_{av}^n - \tau_{wv}^n + \frac{\partial \sigma_{22(P_p^n)}^n}{\partial y} + \frac{\partial \sigma_{12(P_p^n)}^n}{\partial x}, \quad (18)$$

where h, A and P_p are at time level n because BDF2 is used along with IMEX (as explained below).

We note in passing that a second-order Crank-Nicolson scheme for the momentum equation was not successful because the water stress term leads to an an undamped oscillation. For more details, the reader is referred to Appendix A.

Secondly, to obtain second-order accuracy in time for the continuity equations, we use a second-order Runge-Kutta (RK2) predictor-corrector approach to obtain h^n and A^n. Hence, they are obtained in two steps by doing

$$\frac{(h^* - h^{n-1})}{\Delta t/2} + \nabla \cdot (\mathbf{u}_2^{n-1} h^{n-1}) = 0, \quad (19)$$

$$\frac{(h^n - h^{n-1})}{\Delta t} + \nabla \cdot (\mathbf{u}_2^{n-\frac{1}{2}} h^*) = 0, \quad (20)$$

where $\mathbf{u}_2^{n-\frac{1}{2}} = (\mathbf{u}_2^{n-1} + \mathbf{u}_2^n)/2$. h^* is centered in time as $\Delta t/2$ is used to perform the advection for the predictor step. Both steps use the upstream scheme. We introduce the operator $h^n = L_{RK2}(h^{n-1}, \mathbf{u}_2^{n-1}, \mathbf{u}_2^n)$, similar to the one in equation (16), in order to denote the two-step calculation of h^n. The RK2 approach with the upstream scheme has the same CFL condition than the first-order scheme.

Before we introduce our third modification and explain how these equations can be solved simultaneously for u^n, v^n, h^n and A^n, we need to present the JFNK solver.

3.2. Spatial discretization and boundary conditions

The components of the velocity (u and v) are positioned on the Arakawa C-grid. A Dirichlet boundary condition is applied at an ocean-land boundary ($u = 0$, $v = 0$) and a Neumann condition at an open boundary (i.e., the spatial derivatives of the components of velocity in the normal direction with the open boundary are chosen to be zero). Gradients of h and A are also set to zero at an open boundary. For stability, the ice strength P_p is set to zero at the open boundaries [25]. A f-plane approximation is used with $f = 1.46 \times 10^{-4}\mathrm{s}^{-1}$. Spatial derivatives (in the rheology term) are discretized using centered finite differences except close to land boundaries where second order accurate Taylor series expansions are used. As opposed to our work in [4] and [10], the viscous coefficients are calculated following the method described in Bouillon et al. [9]. The spatial discretization (with nx tracer points in one direction and ny in the other one) leads to a system of $N = (ny(nx+1) + nx(ny+1))$ nonlinear equations for the velocity components and $(nx+2)(ny+2)$ equations for each h and A (this includes the boundary conditions).

3.3. The JFNK solver

We give a brief overview of the JFNK implementation. More details can be found in [4, 10, 26]. The u and v equations to be solved at time level n for each grid cell can be written as

$$\frac{\rho h_u^l}{\Delta t}(\alpha u^n + \beta u^{n-1} + \gamma u^{n-2}) = \rho h_u^l f v_{avg}^n + \tau_{au}^n - \tau_{wu}^n + \frac{\partial \sigma_{11(P_p^l)}^n}{\partial x} + \frac{\partial \sigma_{12(P_p^l)}^n}{\partial y}, \quad (21)$$

$$\frac{\rho h_v^l}{\Delta t}(\alpha v^n + \beta v^{n-1} + \gamma v^{n-2}) = -\rho h_v^l f u_{avg}^n + \tau_{av}^n - \tau_{wv}^n + \frac{\partial \sigma_{22(P_p^l)}^n}{\partial y} + \frac{\partial \sigma_{12(P_p^l)}^n}{\partial x}, \quad (22)$$

where h_u is the thickness evaluated at the u location on the C-grid and v_{avg} is the average of the four v components surrounding the u location (similar idea for h_v and u_{avg}). The parameters α, β and γ are respectively equal to 1, -1 and 0 for the SIT approach and to $\frac{3}{2}$, -2 and $\frac{1}{2}$ for the BDF2 scheme. The superscript l is $n-1$ for the SIT method while it is n with the IMEX method (explained below).

From both approaches, we obtain equations that are functions of u^n and v^n. The spatial discretization of equations (21) and (22) leads to a system of N nonlinear equations with N unknowns that can be concisely written as

$$\mathbf{A}_m(\mathbf{u}^n)\mathbf{u}^n = \mathbf{b}(\mathbf{u}^n), \tag{23}$$

where $\mathbf{A}_m$ is an $N \times N$ matrix. We added a subscript m to distinguish the system matrix from the ice concentration vector $\mathbf{A}$. The vector $\mathbf{u}^n$, of size N, is formed by stacking first the u components followed by the v components. The vector $\mathbf{b}$ is a function of the velocity vector $\mathbf{u}^n$ because of the water stress term. Note that the system of equations also depends on the vectors $\mathbf{h}^n$ and $\mathbf{A}^n$ for IMEX and on $\mathbf{h}^{n-1}$ and $\mathbf{A}^{n-1}$ when using the SIT approach. The systems of equations to be solved are different whether the SIT or BDF2 approach is used (the two methods lead to different system matrix, vector $\mathbf{b}$ and solution). We drop the superscript n knowing that we wish to find the solution $\mathbf{u} = \mathbf{u}^n$. We introduce the residual vector $\mathbf{F}(\mathbf{u})$:

$$\mathbf{F}(\mathbf{u}) = \mathbf{A}_m(\mathbf{u})\mathbf{u} - \mathbf{b}(\mathbf{u}). \tag{24}$$

The residual vector $\mathbf{F}(\mathbf{u})$ is useful as it allows one to evaluate the quality of the approximate solution as $\mathbf{F}(\mathbf{u}) = 0$ if the solution is fully converged.

The Newton method is used to solve the nonlinear system of equations given in (23). The iterates obtained during the Newton method are referred to as $\mathbf{u}^k$ where the superscript k corresponds to the Newton iteration number. This nonlinear method is based on a multivariate Taylor expansion around a previous iterate $\mathbf{u}^{k-1}$:

$$\mathbf{F}(\mathbf{u}^{k-1} + \delta\mathbf{u}^k) \approx \mathbf{F}(\mathbf{u}^{k-1}) + \mathbf{F}^{'}(\mathbf{u}^{k-1})\delta\mathbf{u}^k. \tag{25}$$

The higher order terms are neglected in the expression above. Setting $\mathbf{F}(\mathbf{u}^{k-1} + \delta\mathbf{u}^k) = 0$, $\delta\mathbf{u}^k = \mathbf{u}^k - \mathbf{u}^{k-1}$ can be obtained by solving the linear system of N equations:

$$\mathbf{J}(\mathbf{u}^{k-1})\delta\mathbf{u}^k = -\mathbf{F}(\mathbf{u}^{k-1}), \tag{26}$$

where the system matrix $\mathbf{J} \equiv \mathbf{F}^{'}$ is the Jacobian, an $N \times N$ matrix whose entries are $J_{qr} = \partial F_q(\mathbf{u}^{k-1})/\partial(u_r^{k-1})$ (where $q = 1, N$ and $r = 1, N$). For $k = 1$, an initial iterate $\mathbf{u}^0$ needs to be provided. The initial iterate here is the previous time level solution $\mathbf{u}^{n-1}$. Once the linear system of equations (26) is solved, the next iterate is given by

$$\mathbf{u}^k = \mathbf{u}^{k-1} + \lambda\delta\mathbf{u}^k, \tag{27}$$

where $\lambda = \left[1, \frac{1}{2}, \frac{1}{4}, \frac{1}{8}\right]$ is iteratively reduced until $||\mathbf{F}(\mathbf{u^k})|| < ||\mathbf{F}(\mathbf{u^{k-1}})||$ or until $\lambda = \frac{1}{8}$. The symbol $|| \; ||$ denotes the L2-norm. This linesearch approach is an addition compared to the previous model versions described in Lemieux et al. [4] and Lemieux et al. [10] (see also Losch et al. [11]). This method greatly improves the robustness of the nonlinear solver.

The linear system of equations in (26) is solved using the Flexible Generalized Minimum RESidual (FGMRES, [27]) method. Krylov methods such as FGMRES approximates the solution in a subspace of small dimension. When creating the subspace, Krylov methods only need the product of $\mathbf{J}$ times certain vectors (see Knoll and Keyes [28] for details). The Jacobian matrix therefore does not need to be formed per se but only its action on a vector is required. Given a certain vector $\mathbf{w}$ formed during the Krylov process, the product of $\mathbf{J}$ times $\mathbf{w}$ can be approximated by

$$\mathbf{J}(\mathbf{u}^{k-1})\mathbf{w} \sim \frac{\mathbf{F}(\mathbf{u}^{k-1} + \epsilon\mathbf{w}) - \mathbf{F}(\mathbf{u}^{k-1})}{\epsilon}, \tag{28}$$

where ϵ is a small perturbation.

To speed up convergence of the linear solution, the system of equations is transformed using right preconditioning. The preconditioning operator is based on the matrix $\mathbf{A}_m$ linearized with the previous iterate and involves 10 iterations of a Line Successive Over Relaxation (LSOR) scheme [4, 26]. The preconditioning operator is slightly different whether the SIT or the BDF2 method is used. This is a consequence of the different formulation of the inertial term which just leads to a multiplying factor of $\frac{3}{2}$ for BDF2 and of 1 for SIT.

To improve robustness and computational efficiency, an inexact Newton method [29] is employed. With this approach, a loose tolerance is used in early Newton iterations and it is progressively tighten up as the nonlinear solution is approached. The preconditioned FGMRES method solves the linear system of equations until the linear residual is smaller than $\gamma(k) \parallel \mathbf{F}(\mathbf{u}^{k-1}) \parallel$ where $\gamma(k)$ is the tolerance of the linear solver at iteration k (a value smaller than 1). The tolerance of the linear solver with this inexact

Newton approach is given by

$$\gamma(k) = \begin{cases} \gamma_{ini}, & \text{if } ||\mathbf{F}(\mathbf{u^{k-1}})|| \geq \text{r}, \\ \left[\frac{||\mathbf{F}(\mathbf{u^{k-1}})||}{||\mathbf{F}(\mathbf{u^{k-2}})||}\right]^{\alpha}, & \text{if } ||\mathbf{F}(\mathbf{u^{k-1}})|| < \text{r}. \end{cases} \tag{29}$$

The tolerance γ_{ini} for the initial stage is set to 0.99. The exponent α is set to 1.5 and $r = \frac{2}{3}||\mathbf{F}(\mathbf{u^0})||$. Because of the linesearch approach, a more aggressive evolution of the linear tolerance is used compared to the settings in [4, 10]. The tolerance $\gamma(k)$ is also forced to be larger than 0.1 to prevent excessive use of the linear solver which tends to slow down the nonlinear solver. We will get back to this issue later in the paper.

Finally, a termination criterion (defined by γ_{nl}) for solving the nonlinear system of equations is also needed. The JFNK solver stops iterating after the L2-norm of the residual is lower than $\gamma_{nl}||\mathbf{F}(\mathbf{u^0})||$. JFNK fails to converge when the termination criterion is not reached in k_{max}=100 iterations.

The JFNK algorithm with the SIT approach and the first-order upstream scheme is:

`1.  Start with an initial iterate` $\mathbf{u}^0$

`do` $k = 1,\ k_{max}$

  `2.  ''Solve''` $\mathbf{J}(\mathbf{u}^{k-1})\delta\mathbf{u}^k = -\mathbf{F}(\mathbf{u}^{k-1})$ `with FGMRES`

  `3.` $\mathbf{u}^k = \mathbf{u}^{k-1} + \lambda\delta\mathbf{u}^k$

  `4.  If` $||\mathbf{F}(\mathbf{u}^k)|| < \gamma_{nl}||\mathbf{F}(\mathbf{u}^0)||$ `stop`

`enddo`

5. Calc $\mathbf{h}^n = L(\mathbf{h}^{n-1}, \mathbf{u}^n)$ and $\mathbf{A}^n = L(\mathbf{A}^{n-1}, \mathbf{u}^n)$

where the initial iterate $\mathbf{u}^0$ is the previous time level solution and $\mathbf{u}^k = \mathbf{u}^n$ once it has converged. The matrix $\mathbf{J}$ and the vector $\mathbf{F}$ are functions of $\mathbf{h}$ and $\mathbf{A}$ at the previous time level, i.e. $\mathbf{h}^{n-1}$ and $\mathbf{A}^{n-1}$ (note that SIT is technically an IMEX method, but it is not iterated).

The iterated IMEX approach (simply referred to as IMEX) now allows one to solve for $\mathbf{u}^n$, $\mathbf{v}^n$, $\mathbf{h}^n$ and $\mathbf{A}^n$ simultaneously. In order to do this, the explicit calculations of the thickness and concentration are moved inside the Newton loop.

1. Start with an initial iterate $\mathbf{u}^0$
do $k = 1,\ k_{max}$
   2. Calc $\mathbf{h}^k = L(\mathbf{h}^{n-1}, \mathbf{u}^{k-1})$ and $\mathbf{A}^k = L(\mathbf{A}^{n-1}, \mathbf{u}^{k-1})$
   3. ''Solve'' $\mathbf{J}(\mathbf{u}^{k-1})\delta\mathbf{u}^k = -\mathbf{F}(\mathbf{u}^{k-1})$ with FGMRES
   4. $\mathbf{u}^k = \mathbf{u}^{k-1} + \lambda\delta\mathbf{u}^k$
   5. If $||\mathbf{F}(\mathbf{u}^k)|| < \gamma_{nl}||\mathbf{F}(\mathbf{u}^0)||$ stop
enddo

where in this case $\mathbf{J}$ and $\mathbf{F}$ are function of $\mathbf{h}^k$ and $\mathbf{A}^k$.

To obtain second-order accuracy in time, the latter algorithm can be modified by using the L_{RK2} advection operator and by using the BDF2 method. Hence, the BDF2-IMEX-RK2 algorithm is given by

1. Start with an initial iterate $\mathbf{u}^0$
do $k = 1,\ k_{max}$
   2. Calc $\mathbf{h}^k = L_{RK2}(\mathbf{h}^{n-1}, \mathbf{u}^{n-1}, \mathbf{u}^{k-1})$ and $\mathbf{A}^k = L_{RK2}(\mathbf{A}^{n-1}, \mathbf{u}^{n-1}, \mathbf{u}^{k-1})$
   3. ''Solve'' $\mathbf{J}(\mathbf{u}^{k-1})\delta\mathbf{u}^k = -\mathbf{F}(\mathbf{u}^{k-1})$ with FGMRES
   4. $\mathbf{u}^k = \mathbf{u}^{k-1} + \lambda\delta\mathbf{u}^k$
   5. If $||\mathbf{F}(\mathbf{u}^k)|| < \gamma_{nl}||\mathbf{F}(\mathbf{u}^0)||$ stop
enddo

To ensure fast nonlinear convergence in the context of the IMEX or BDF2-IMEX-RK2 scheme, it is crucial to take into account the change in $\mathbf{h}$ and $\mathbf{A}$ associated with a change of velocity in the evaluation of $\mathbf{J}$ times a certain Krylov vector $\mathbf{w}$ (equation (28)). Hence, with the BDF2-IMEX-RK2 scheme, $\mathbf{F}(\mathbf{u}^{k-1} + \epsilon\mathbf{w})$ is a function of $\mathbf{h}^+ = L_{RK2}(\mathbf{h}^{n-1}, \mathbf{u}^{n-1}, \mathbf{u}^+)$ and $\mathbf{A}^+ = L_{RK2}(\mathbf{A}^{n-1}, \mathbf{u}^{n-1}, \mathbf{u}^+)$ where $\mathbf{u}^+$ is $\mathbf{u}^{k-1} + \epsilon\mathbf{w}$ (same idea for IMEX by using the simpler operator L).

For simplicity, the same notation is used for the three algorithms given above. However, as they do not solve the same nonlinear systems of equations, they lead to different Jacobian matrices, residual vectors and solutions.

A truncation error analysis, that demonstrates second-order accuracy in time for BDF2-IMEX-RK2, is given in Appendix B.

Symbol	Definition	value
ρ	sea ice density	900 kg m^{-3}
ρ_a	air density	1.3 kg m^{-3}
ρ_w	water density	1026 kg m^{-3}
C_{da}	air drag coefficient	1.2×10^{-3}
C_{dw}	water drag coefficient	5.5×10^{-3}
θ_{da}	air turning angle	25°
θ_{dw}	water turning angle	25°
f	Coriolis parameter	$1.46 \times 10^{-4} s^{-1}$
P*	ice strength parameter	27.5×10^3 N m^{-2}
C	ice concentration parameter	20
e	ellipse ratio	2

Table 1: Physical parameters for the numerical simulations

4. Information about the model

Our pan-Arctic regional model can be run at four possible spatial resolutions: 10, 20, 40 and 80 km (square cartesian grids). The model uses two thickness categories and a zero-layer thermodynamics (described in [3]). The sea ice model is coupled thermodynamically to a slab ocean model. Climatological ocean currents are used to force the sea ice model and to advect heat in the ocean. The wind stress is calculated using the geostrophic winds derived from the National Centers for Environmental Prediction and National Center for Atmospheric Research (NCEP/NCAR) six hour reanalysis of sea level pressure [30].

Tables (1) lists the values of the physical parameters used for the simulations in this paper.

For all the 2-D experiments, we use revision 317 of our model with small modifications to perform the experiments described below. The code is serial. All runs were performed on a machine with 2 Intel E5520 quad-core CPU at 2.26 GHz with 8 MB of cache and 72 GB of RAM. The compiler is GNU fortran (GCC) 4.1.2 20080704 (Red Hat 4.1.2-54), 64 bits. The optimization option O3-ffast-math was used for all the runs.

To introduce and better illustrate the SIT instability, a few 1-D experiments are performed. Revision 89 of our 1-D model is used for all the 1-D experiments. A detailed description of the sea ice dynamic equations in 1-D can be found in [2].

5. Results

A series of one day numerical experiments in 1-D and 2-D are performed for the different time integration schemes at spatial resolutions of 40 and 20 km. The base set of numerical experiments use the SIT algorithm (referred to as SIT). The second set of numerical experiments use the iterated IMEX algorithm (referred to as IMEX). The final set of numerical experiments use the BDF2 scheme along with IMEX and the RK2 advection scheme (referred to as BDF2-IMEX-RK2). For each series, one day experiments are performed with different time steps (Δt). To ensure that the CFL condition is respected, the maximum Δt at 40-km resolution is set to 360 min while it is 180 min for a resolution of 20 km (At these resolutions and maximum time steps, the CFL criterion is not violated for ice velocities ≤ 1 ms^{-1}).

It was observed that the solver had difficulties at the beginning of the time integration (with small wind and ice starting from rest). A value of $\epsilon = 10^{-7}$, in the evaluation of the Jacobian times a vector (equation (28)), improves robustness compared to the value of 10^{-6} used in [4, 10]. Robustness was improved for the first few time levels by setting $\epsilon = 10^{-8}$ instead of 10^{-7} when the Newton iteration is larger than 50. This robustness issue is not a major problem as it has not been observed in realistic experiments. It is possible that a more sophisticated way of choosing ϵ (as described in [28]) or an exact Jacobian-times-vector operation by automatic differentiation [11] could improve robustness for these idealized experiments, but this is not explored in this paper. As these few initial time levels are not representative of the usual behavior of the solver, only the last 12 hours of the one day integration are used to compute metrics to compare the different time integration approaches.

5.1. 1-D experiments

For these 1-D experiments, the domain is 2000 km long with solid walls at both ends. There is a no inflow/outflow condition at the walls: i.e., the velocity is zero. The spatial resolution is 20 km. The initial thickness field is 1 m everywhere and the sea ice concentration is 0.95. The ice starts from rest. The westerly wind is zero at the beginning and is increased smoothy according to $\mathbf{u}_a^g(t) = (1 - e^{-t/\tau})\mathbf{u}_a^{g*}$ with τ, a time constant set to 6 hours, and $|\mathbf{u}_a^{g*}|$ =10 m s^{-1} being the same everywhere.

To assess the quality of these approximate solutions, a 24-h reference solution is obtained by using a time step of 1 s (with BDF2-IMEX-RK2). We then compare the 24-h sea ice thickness field obtained with an integration scheme using a certain Δt with the reference solution. Thickness is used because it acts as an integrator of all the errors produced during the time integration. The Root Mean Square Error (RMSE) between a thickness field and the reference thickness field is calculated for all the experiments. The RMSE should decrease with Δt for all three series of experiments. BDF2-IMEX-RK2 should be the most accurate and lead to second-order accuracy in time while the other two series (SIT and IMEX) are expected to be first-order accurate in time. The termination criterion is $\gamma_{nl} = 10^{-6}$ for all the experiments.

Fig. 1a indeed confirms that SIT and IMEX are both first order accurate in time (the slope is $\sim$1 on a log-log plot). This figure shows the RMSE between an approximate solution (thickness) and the reference solution as a function of the time step. Despite some wiggling, BDF2-IMEX-RK2 exhibits second-order accuracy in time. For any Δt, the BDF2-IMEX-RK2 solution is more than one order of magnitude more accurate than the IMEX and SIT ones. The improvement of IMEX over SIT is small except for large Δt. This implies that for smaller Δt, the splitting errors are smaller than the standard first-order discretization errors. The sudden increase in the RMSE for SIT for Δt larger than 60 min is due to noise in the thickness field near both walls.

The fact that the approximate solution for SIT is contaminated by noise makes it more difficult for JFNK to obtain the velocity field solution. This is illustrated in Fig. 1b. Whereas both IMEX and BDF2-IMEX-RK2 need less than 20 Newton iterations (on average), SIT behaves differently than these two schemes for Δt larger than 15 min. Indeed, the mean number of Newton iterations for SIT increases significantly for $\Delta t > 15$ min. There was even a failure of JFNK for $\Delta t = 120$ min.

These additional Newton iterations for SIT have an impact on the total CPU time as can be seen in Fig. 1c. While SIT is more efficient than IMEX and BDF2-IMEX-RK2 for small Δt, the additional Newton iterations for $\Delta t > 15$ min causes SIT to be more costly. Hence, BDF2-IMEX-RK2 is always significantly more accurate than SIT and it is also more computationally efficient than SIT for typical time steps (e.g. $\Delta t = 60$ min).

Fig. 2 displays how the errors are spatially distributed. The reference thickness and velocity solutions are respectively shown on Fig. 2a and 2b. The ice has piled up and the velocity exhibits strong convergence at the wall. The ice concentration has reached 1.0 close to the wall (not shown).

The difference between the thickness obtained with SIT when using a time step of 120 min or 180 min and the reference solution are respectively shown on Fig. 2c and Fig. 2d in black. Similar to the results of Lipscomb et al. [2], there is noise in the approximate solution in the region of convergence. It is also observed that errors are also present on the western side of the domain where the ice is diverging. The error is, however, more localized than close to the eastern wall. The maximum errors are respectively 2.5 cm and 8.1 cm for Δt of 120 and 180 min. These figures also demonstrate that the noise is notably smaller everywhere on the domain with BDF2-IMEX-RK2 (in blue). In this case, the maximum errors are 0.1 cm ($\Delta t = 120$ min) and 0.32 cm ($\Delta t = 180$ min). As opposed to the SIT scheme, the IMEX approach decreases the errors close to the eastern wall but does not significantly affect the noise on the other side of the domain where the ice diverges (not shown).

5.2. 2-D experiments

Experiments in 2-D are performed at 40 and 20-km resolutions. The initial conditions for these one day are the same than in [10]. These experiments are performed starting on 17 January 2002 00Z. As in Lemieux et al. [10], this 24-hour period was chosen because it is characterized by typical conditions in the Arctic: a high pressure system close to the Beaufort Sea, convergence north of Greenland and ice flowing south through Fram Strait. The thermodynamics and the ocean currents are set to zero for these idealized experiments. The ice starts from rest. It is then accelerated by a smoothly

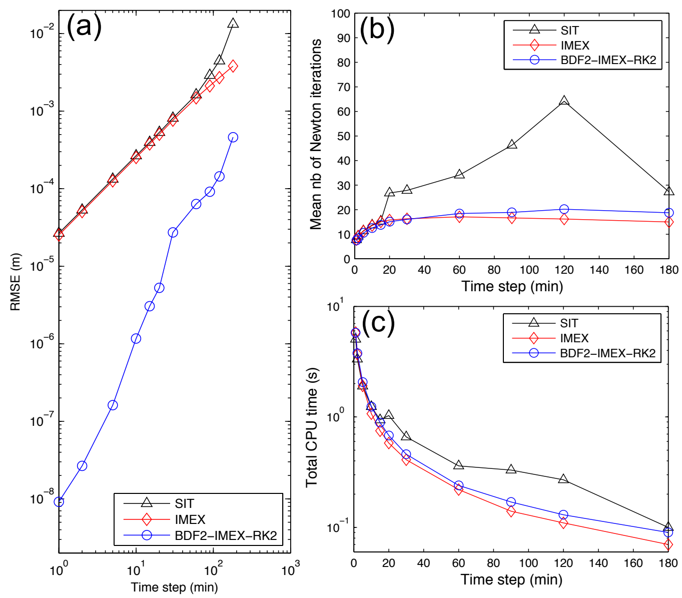

Figure 1: RMSE (a), mean number of Newton iterations per time level (b) and total CPU time (c) as a function of the time step. The mean number of Newton iterations and total CPU time were calculated for the last 12 h of the integration. Black curve with triangles is for the SIT scheme, red curve with diamonds is for IMEX while the blue curve with circles is BDF2-IMEX-RK2. This is a 1-D experiment with a spatial resolution of 20 km.

increased wind stress field. The geostrophic wind field on 18 January 2002 00Z is used but it is ramped up according to

$$\mathbf{u}_a^g(t) = (1 - e^{-t/\tau})\mathbf{u}_a^{g*}, \tag{30}$$

where $\mathbf{u}_a^{g*}$ is the geostrophic wind field on 18 January 2002 00Z, t is the time (starting on 17 January 2002 00Z) and τ is set to 6 hours as in the 1-D experiments.

A reference solution is again obtained by using a time step of 1 s (with BDF2-IMEX-RK2). We then compare the sea ice thickness field obtained on 18 January 2002 00Z with the reference solution valid at the same time. As in the 1-D experiments, the termination criterion is set to $\gamma_{nl} = 10^{-6}$.

Fig. 3a shows the 20-km reference solution concentration field on 18 January 2002 00Z while Fig. 3b displays the reference solution velocity field at

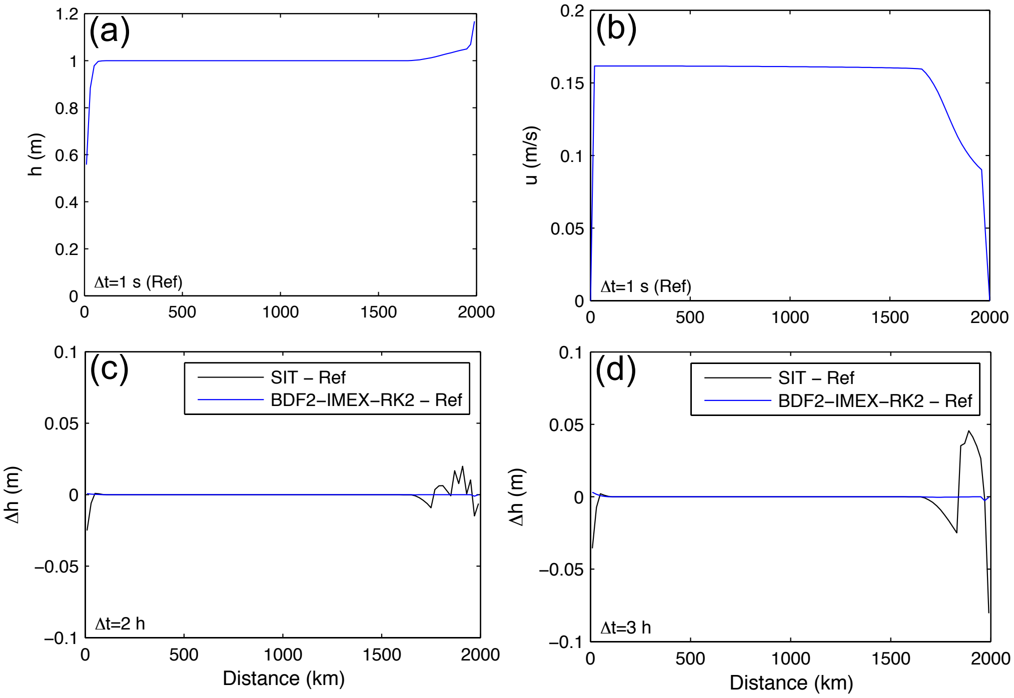

Figure 2: 1-D reference solution ice thickness (a) and velocity (b) fields. Difference between the thickness field obtained with the SIT approach (in black) or with BDF2-IMEX-RK2 (in blue) and the reference solution for $\Delta t = 120$ min (c) and $\Delta t = 180$ min (d). The spatial resolution is 20 km. The x-axis for these graphs is the distance in km from the western wall.

the same valid time. The reference thickness solution is shown in Fig. 7a.

Fig. 4 shows, for the different schemes, the RMSE as a function of the time step on a log-log plot for spatial resolutions of 40 km (a) and 20 km (b). The RMSE is calculated only where the concentration of the reference solution is above 50%. The behavior of the time integration scheme is qualitatively the same at both resolutions. We therefore concentrate on the 20-km resolution results. The SIT and IMEX schemes lead to first-order accuracy in time while BDF2-IMEX-RK2 clearly demonstrates that it is second-order accurate in time over a wide range of Δt. There seems to be error saturation for large Δt as a flattening of the curve is observed.

As the continuity and momentum equations are solved simultaneously

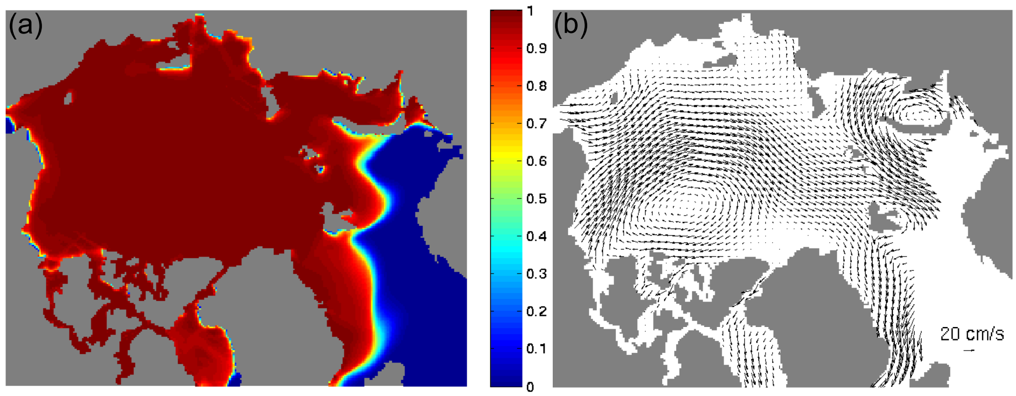

Figure 3: Ice concentration (a) and velocity field (b) at 20-km resolution on 18 January 2002 00Z obtained with BDF2-IMEX-RK2 with a time step of 1 s. These 2-D fields form the reference solution. For clarity, only one velocity vector out of 16 is shown. The continents are in gray.

with BDF2-IMEX-RK2, we verify that the scheme also leads to second-order accuracy in time for the velocity field. Fig. 5 shows the RMS of the magnitude of the velocity error (referred to as RMSEv) between an approximate solution and the reference solution as a function of Δt. This result demonstrates second-order accuracy in time for the velocity field when using the BDF2-IMEX-RK2 scheme.

Consistent with the findings of Lipscomb et al. [2], we observe that SIT is less sensitive in 2-D than in 1-D. Shear stress tends to help the numerical scheme. A test with an elliptical yield curve with a very large aspect ratio of 1000 (i.e., with very small resistance to shear deformations) shows that results in 2-D exhibit a similar behavior to results in 1-D (the mean number of Newton iterations and RMSE for SIT increases significantly for large Δt, not shown). Our results also suggest that our model is less sensitive to the SIT instability than the one of Lipscomb et al. [2]. This is likely because we use a two-thickness category model as opposed to their multi-category model.

Fig. 6a and Fig. 6b respectively show the mean number of Newton iterations per time level (last 12 h) and the total CPU time required for the last 12 h of the one day integration, as a function of Δt, for the different time integration schemes. As opposed to the 1-D experiments, the number of Newton iterations for SIT is about the same as for IMEX and BDF2-

IMEX-RK2 even for large Δt. BDF2-IMEX-RK2 requires roughly 10-25% more total CPU time than SIT for the same Δt. As this is not due to an increase in the number of Newton iterations (the number is even slightly lower for BDF2-IMEX-RK2), the extra CPU time for BDF2-IMEX-RK2 is rather a consequence of the additional operations inside the Newton loop (the two-step advection operator). However, comparing the computational efficiency of SIT and BDF2-IMEX-RK2 for the same Δt is not a fair comparison as the integration schemes do not lead to the same accuracy. As an example, BDF2-IMEX-RK2 with a Δt of 90 min leads to an approximate solution that is more accurate (RMSE of 1.77×10^{-4} m) than the one obtained with SIT with Δt= 10 min (RMSE of 2.86×10^{-4} m, Fig. 4b). As the total CPU time required by BDF2-IMEX-RK2 with Δt= 90 min is 146 s and the one for SIT with Δt= 10 min is 775 s, this means that the second-order scheme is more than five times faster than the SIT integration scheme to obtain the same accuracy.

Fig. 7c shows how the thickness errors are spatially distributed on the pan-Arctic domain when using BDF2-IMEX-RK2 with Δt=90 min. This can be compared to the errors obtained with SIT for the same Δt of 90 min (Fig. 7b). Fig. 7b shows that notable errors are found at many places in the domain, with the largest errors close to the coast lines. The largest errors in SIT with Δt=90 min is -7.6 cm while the maximum error is reduced to 0.34 cm with BDF2-IMEX-RK2 when using the same time step. As mentioned earlier, SIT needs a Δt=10 min to obtain a comparable RMSE than the one obtained with BDF2-IMEX-RK2 with Δt=90 min. The spatial errors for SIT for a Δt of 10 min are shown on Fig. 7d. Qualitatively speaking, it can be observed that the errors in Fig. 7c and Fig. 7d are of similar magnitude, although the spatial patterns are different. The largest error for SIT with Δt=10 min is -0.78 cm.

5.3. Robustness

We have first assessed the robustness of the BDF2-IMEX-RK2 scheme when using winds that change more abruptly. We repeated the 40 km resolution experiments of Section 5.2 but with winds that change a lot more quickly. The time constant in equation (30), that determines how quickly the winds are ramped up, was set to 1 hour (instead of 6 hours). Results demonstrate that the BDF2-IMEX-RK2 scheme still leads to second-order accuracy in time (not shown).

We have also investigated how robust is our JFNK solver when used in the context of the BDF2-IMEX-RK2 scheme or in the context of the SIT first-order approach. We ran the 2-D model for five years (2002-2007) at 40 and 20-km resolutions with either BDF2-IMEX-RK2 or SIT and counted the number of failures of JFNK. For all these experiments, Δt is 30 min and $\gamma_{nl} = 10^{-4}$. Note that realistic wind forcing was used and thermodynamic source terms were included (through operator splitting) for these long simulations.

The introduction of the linesearch globalization and to a lesser extent of the Bouillon et al. [9] approach for the calculation of the viscous coefficients clearly improved the robustness of our JFNK solver when compared to the first version described in [4]. For these five-year integrations, JFNK within both the SIT and BDF2-IMEX-RK2 schemes did not fail at 40-km resolution. However, at 20-km resolution, JFNK failed a few times for both integration schemes. In terms of percentage, the failure rate is 0.027 % for SIT while it is 0.025 % for BDF2-IMEX-RK2. Losch et al. [11] report a failure rate of 0.006% with a SIT approach over a 50 year simulations for a spatial resolution of 27 km.

6. Discussion and concluding remarks

To our knowledge, we have demonstrated for the first time second-order temporal accuracy in a sea ice dynamic model. This second-order scheme was implemented relatively easily from a Splitting In Time (SIT) scheme using a Jacobian-free Newton-Krylov (JFNK) nonlinear solver. Basically, three minor modifications were made to this configuration to get second-order accuracy in time. First, the advection operation was moved inside the Newton loop such that the ice thickness and concentration fields are updated along with the velocity field during the Newton iteration. Secondly, the first-order explicit advection operation was upgraded to a second-order Runge-Kutta (RK2) predictor-corrector approach. Finally, in order to get second-order accuracy, the backward Euler time discretization in the momentum equation was replaced by a second-order backward difference formula (BDF2) integration scheme. We refer to this new iterated IMplicit-EXplicit (IMEX) scheme as BDF2-IMEX-RK2. This implementation is a lot more straightforward than the development of a fully implicit scheme would have been.

The Root Mean Square Error (RMSE) between thickness fields obtained with different time steps (Δt) and a reference solution thickness field demonstrates that BDF2-IMEX-RK2 is second-order accurate in time. The supporting analysis can be found in Appendix B. Results at 40 and 20-km resolutions lead qualitatively to the same conclusions. For the same Δt, BDF2-IMEX-RK2 is always more than one order of magnitude more accurate than the SIT approach. As an example, the approximate solution obtained with BDF2-IMEX-RK2 with Δt= 90 min is more accurate than the one obtained with SIT with Δt=10 min. Hence, to get the same level of accuracy than SIT, significantly larger time steps can be used with BDF2-IMEX-RK2 which leads to a decrease in the computational time. This efficiency gain is greater than a factor of 5 at 20-km resolution.

The implementation of this efficient second-order accurate in time scheme was possible because our nonlinear solver for the momentum equation is a Newton-Krylov scheme. As the EVP solver [8] is an explicit scheme, the IMEX approach would not be possible with this method. On the other hand, IMEX could be implemented in the framework of a Picard iteration (e.g. [5, 6, 7]) although the Picard solver is known to exhibit a very inefficient nonlinear convergence [7, 11].

To maintain the fast nonlinear convergence of JFNK with the IMEX approach, it is crucial to take into account the changes in thickness and concentration associated with a change of velocity when performing the calculation of the Jacobian times a vector. This operation is performed correctly in our BDF2-IMEX-RK2 as can be seen in Fig. 6a. This figure shows that the mean number of Newton iterations is about the same with BDF2-IMEX-RK2 than it is with the SIT scheme (it is even a little lower). To reinforce this conclusion, we show in Fig. 8 a typical nonlinear evolution of the L2-norm of the residual for BDF2-IMEX-RK2 and for the SIT schemes. The time step is 30 min and the resolution is 20 km. Both schemes exhibit a very similar nonlinear convergence. They both need 12 Newton iterations to reach the nonlinear convergence criterion ($\gamma_{nl} = 10^{-6}$).

As in Lipscomb et al. [2], we found that the 2-D model is less sensitive than the 1-D model to the SIT instability. The BDF2-IMEX-RK2 scheme is nevertheless useful as the SIT instability is more severe as the grid is refined and when using a multi-category sea ice model [2]. Note that our method could easily be applied to a multi-category model. Furthermore, a sea ice model using a yield curve having less shear strength than the standard elliptical yield curve would also be more exposed to this instability and would therefore benefit from the more stable BDF2-IMEX-RK2 scheme.

An obvious extension to this work would be to develop a second-order scheme that would also include thermodynamic processes. To do so, the predictor-corrector approach would include the source terms and would become

$$\frac{(h^* - h^{n-1})}{\Delta t/2} = -\nabla \cdot (\mathbf{u}^{n-1}h^{n-1}) + S_h(h^{n-1}, A^{n-1}), \tag{31}$$

$$\frac{(h^n - h^{n-1})}{\Delta t} = -\nabla \cdot (\mathbf{u}^{n-\frac{1}{2}}h^*) + S_h(h^*, A^*), \tag{32}$$

where A^* and A^n would be obtained in a similar way.

Another improvement would be to replace our diffusive first-order in space upstream scheme by a more sophisticated advection operator. For example, second-order accuracy in space could also be achieved by using the remapping scheme of Lipscomb and Hunke [31]. Note that a stabilization method (different time-stepping approach) may be required as higher order advection schemes are less diffusive than a first-order upstream operator.

The JFNK solver is remarkably robust in longer simulations (five years). At 40-km resolution, JFNK did not fail for either the SIT or the BDF2-IMEX-RK2 integration scheme. At 20-km resolution, convergence was not reached on rare occasions for both integration schemes. With SIT, JFNK had a failure rate as low as 0.027 % while JFNK with the BDF2-IMEX-RK2 scheme failed for only 0.025 % of the time levels (this is slightly smaller than for SIT but probably not statistically significant).

Even though these failure rates are very small and when a failure occurs it usually affects only a few grid cells (not shown), the increase in the failure rates with resolution indicates that further work is needed to improve the robustness. A more sophisticated approach than the linesearch method might help (e.g. [32]) but we also suspect that our preconditioning approach might need to be revisited as we refine the grid.

Indeed, as the spatial resolution increases, the rheology term makes the problem more and more nonlinear. We have observed occasional failures of the preconditioned FGMRES at 10-km resolution for a linear tolerance γ of 0.1. To improve our preconditioning operator, we are currently working on using the MultiLevel (ML) preconditioner from the Trilinos library [33]. It is possible, however, that this might not be sufficient and that we might have to reconsider the use of the Picard matrix for the preconditioning step. In other words, our preconditioning matrix might have to be closer to the Jacobian matrix than what the Picard matrix is.

This study was done using a serial code. Losch et al. [11] have recently implemented a parallel JFNK solver for sea ice dynamics. They have demonstrated that the scaling of JFNK with a similar line relaxation approach for the preconditioner is almost as good as for other solvers (Picard and EVP); in their case for domain decompositions of up to 1000 CPUs. There is no reason to believe that our BDF2-IMEX-RK2 approach would not exhibit similar performances as the additional thickness and concentration calculations performed in the Newton loop are explicit and do not require extra communication overheads. Using a different preconditioner (such as ML) might lead to an improved scalability of JFNK. This is the subject of future work.

Appendix A: Undamped oscillation with a Crank-Nicolson approach

By centering in time (at $n-\frac{1}{2}$) the terms in the momentum equation, a Crank-Nicolson approach also leads to second-order accuracy (not shown). However, as explained here, it can lead to an undamped oscillation in zones with little ice. With this approach, the u and v equations are written as

$$\rho h^{n-\frac{1}{2}} \frac{(u^n - u^{n-1})}{\Delta t} = \rho h^{n-\frac{1}{2}} f v^{n-\frac{1}{2}} + \tau_{au}^{n-\frac{1}{2}} - \tau_{wu}^{n-\frac{1}{2}} + \frac{\partial \sigma_{11}^{n-\frac{1}{2}}(P_p^{n-\frac{1}{2}})}{\partial x} + \frac{\partial \sigma_{12}^{n-\frac{1}{2}}(P_p^{n-\frac{1}{2}})}{\partial y}, \tag{33}$$

$$\rho h^{n-\frac{1}{2}}\frac{(v^n - v^{n-1})}{\Delta t} = -\rho h^{n-\frac{1}{2}} f u^{n-\frac{1}{2}} + \tau_{av}^{n-\frac{1}{2}} - \tau_{wv}^{n-\frac{1}{2}} + \frac{\partial \sigma_{22}^{n-\frac{1}{2}}(P_p^{n-\frac{1}{2}})}{\partial y} + \frac{\partial \sigma_{12}^{n-\frac{1}{2}}(P_p^{n-\frac{1}{2}})}{\partial x}, \tag{34}$$

where $h^{n-\frac{1}{2}} = \frac{h^n + h^{n-1}}{2}$ and $A^{n-\frac{1}{2}}$, $u^{n-\frac{1}{2}}$ and $v^{n-\frac{1}{2}}$ are similarly defined. Note that the σ_{ij} and the water stress components are functions of $u^{n-\frac{1}{2}}$ and $v^{n-\frac{1}{2}}$ and that $P_p^{n-\frac{1}{2}} = P^* h^{n-\frac{1}{2}} \exp[-C(1 - A^{n-\frac{1}{2}})]$.

Assuming a region with very thin ice, the balance of force is then between the water stress and the wind stress. To explain the oscillation, we further simplify the problem by setting the water turning angle to zero and by assuming that the ocean is at rest and that the wind is blowing from the west (such that the ice velocity is positive). The momentum balance then becomes

$$\tau_{au}^{n-\frac{1}{2}} = \rho_w C_{dw} (\frac{u^n + u^{n-1}}{2})^2, \tag{35}$$

Assume that the wind stress was zero before such that $u^{n-1} = 0$ and that after that it is constant and equal to τ_{au}. The velocity at time level n is then

$$u^n = 2\sqrt{\frac{\tau_{au}}{\rho_w C_{dw}}}, \tag{36}$$

while at $n + 1$ it is equal to

$$u^{n+1} = 2\sqrt{\frac{\tau_{au}}{\rho_w C_{dw}}} - u^n = 0, \tag{37}$$

and we find that $u^{n+2} = u^n$, i.e., the solution oscillates between two values: 0 and $2\sqrt{\frac{\tau_{au}}{\rho_w C_{dw}}}$. This undamped oscillation is more severe when using large time steps as a significant time difference between two time levels is more likely to lead to a large change in the wind stress. This oscillation is not observed when using the second-order backward difference time integration approach.

Appendix B: Truncation error analysis

We perform a truncation error analysis similar to the one described in Kadioglu and Knoll [14]. We assume a 1-D problem, that the velocity is positive, that the concentration is 1 everywhere and that the viscous coefficients are constant in space and in time. The replacement closure (equation (9)) is not used such that $P = P_p$. We also assume that the Newton iteration has already converged such that $u^k = u^n$ and $h^k = h^n$. The momentum equation is then given by

$$\rho h \frac{\partial u}{\partial t} = R = \tau_a - Cu^2 + \zeta \frac{\partial^2 u}{\partial x^2} - \frac{1}{2}\frac{\partial P}{\partial x}, \tag{38}$$

where $C = \rho_w C_{dw}$, $P = P^* h$ and R is just the sum of all the terms on the RHS. To simplify the notation, we introduce $L_u(u) = \frac{\partial^2 u}{\partial x^2}$ and $L_p(P) = \frac{\partial P}{\partial x}$. The continuity equation for h is

$$\frac{\partial h}{\partial t} = -\frac{\partial (uh)}{\partial x}, \tag{39}$$

for which we introduce the operator $L_{uh}(uh) = \frac{\partial(uh)}{\partial x}$.

At time level n we solve with our BDF2-IMEX-RK2 method the following equations

$$\rho h^n \left(\frac{3u^n}{2} - 2u^{n-1} + \frac{u^{n-2}}{2}\right) = \Delta t R^n, \tag{40}$$

$$h^n = h^{n-1} - \Delta t L_{uh}(u^{n-\frac{1}{2}} h^*), \tag{41}$$

with $u^{n-\frac{1}{2}}$ and h^* given by

$$u^{n-\frac{1}{2}} = \frac{(u^n + u^{n-1})}{2}, \tag{42}$$

$$h^* = h^{n-1} - \frac{\Delta t}{2} L_{uh}(u^{n-1} h^{n-1}). \tag{43}$$

We use the following Taylor series to express u^n as a function of u^{n-1}

$$u^n = u^{n-1} + \Delta t \frac{\partial u^{n-1}}{\partial t} + \frac{\Delta t^2}{2}\frac{\partial^2 u^{n-1}}{\partial t^2} + O(\Delta t^3). \tag{44}$$

We now prove that our BDF2-IMEX-RK2 method leads to second-order accuracy in time for the calculation of the velocity and the thickness. If h and u are both second-order accurate in time, their product is also second-order accurate in time. We can demonstrate this by starting from equation (40) and then by using the other equations we introduced above (the LHS of equation (40) is expressed in terms of products of h and u). Using equation (44) and also a Taylor expansion around u^{n-1} for u^{n-2}, the LHS of equation (40) can be written as

$$\begin{aligned}&\rho h^n \frac{3}{2}(u^{n-1} + \Delta t \frac{\partial u^{n-1}}{\partial t} + \frac{\Delta t^2}{2}\frac{\partial^2 u^{n-1}}{\partial t^2}) - \rho h^n 2u^{n-1} + \\ &\rho h^n \frac{1}{2}(u^{n-1} - \Delta t \frac{\partial u^{n-1}}{\partial t} + \frac{\Delta t^2}{2}\frac{\partial^2 u^{n-1}}{\partial t^2}) + O(\Delta t^3),\end{aligned} \tag{45}$$

which after regrouping the terms becomes

$$\rho h^n \left[\Delta t \frac{\partial u^{n-1}}{\partial t} + \Delta t^2 \frac{\partial^2 u^{n-1}}{\partial t^2} + O(\Delta t^3)\right]. \tag{46}$$

Substituting h^n from equation (41) in (46) we get

$$\rho \left[h^{n-1} - \Delta t L_{uh}(u^{n-\frac{1}{2}} h^*)\right] \left[\Delta t \frac{\partial u^{n-1}}{\partial t} + \Delta t^2 \frac{\partial^2 u^{n-1}}{\partial t^2} + O(\Delta t^3)\right]. \tag{47}$$

From the latest equation, the truncation error (τ_ϵ) can be obtained by subtracting the RHS of equation (40) from expression (47)

$$\tau_\epsilon = \rho \left[h^{n-1} - \Delta t L_{uh}(u^{n-\frac{1}{2}} h^*)\right] \left[\Delta t \frac{\partial u^{n-1}}{\partial t} + \Delta t^2 \frac{\partial^2 u^{n-1}}{\partial t^2} + O(\Delta t^3)\right] - \Delta t R^n, \tag{48}$$

where R^n is expanded below. The terms can be rearranged such that one obtains

$$\tau_\epsilon = \Delta t \rho h^{n-1} \frac{\partial u^{n-1}}{\partial t} + \Delta t^2 \rho h^{n-1} \frac{\partial^2 u^{n-1}}{\partial t^2} - \Delta t^2 \rho L_{uh}(u^{n-\frac{1}{2}} h^*) \frac{\partial u^{n-1}}{\partial t} + O(\Delta t^3) - \Delta t R^n. \tag{49}$$

Using equations (41) and (44) and introducing a Taylor series for the wind stress, R^n can be written as

$$
\begin{aligned}
R^n =& \tau_a^{n-1} + \Delta t \frac{\partial \tau_a^{n-1}}{\partial t} - C\left[(u^{n-1})^2 + 2\Delta t u^{n-1}\frac{\partial u^{n-1}}{\partial t}\right] + \zeta L_u(u^{n-1}) \\
&+ \Delta t \zeta L_u(\frac{\partial u^{n-1}}{\partial t}) - \frac{P^*}{2} L_p(h^n) + O(\Delta t^2).
\end{aligned} \tag{50}
$$

Using again equation (41) for h^n, we get

$$
\begin{aligned}
R^n =& \tau_a^{n-1} + \Delta t \frac{\partial \tau_a^{n-1}}{\partial t} - C\left[(u^{n-1})^2 + 2\Delta t u^{n-1}\frac{\partial u^{n-1}}{\partial t}\right] + \zeta L_u(u^{n-1}) \\
&+ \Delta t \zeta L_u(\frac{\partial u^{n-1}}{\partial t}) - \frac{P^*}{2} L_p(h^{n-1}) + \frac{\Delta t P^*}{2} L_p\left[L_{uh}(u^{n-\frac{1}{2}} h^*)\right] + O(\Delta t^2),
\end{aligned} \tag{51}
$$

Simplifying and using $L_{uh}(u^{n-\frac{1}{2}} h^*) = L_{uh}(u^{n-1}h^{n-1}) + O(\Delta t)$ in equation (51) we get

$$
\begin{aligned}
R^n =& R^{n-1} + \Delta t \frac{\partial \tau_a^{n-1}}{\partial t} - 2\Delta t C u^{n-1}\frac{\partial u^{n-1}}{\partial t} \\
&+ \Delta t \frac{\partial}{\partial t}\zeta L_u(u^{n-1}) - \frac{\Delta t P^*}{2} L_p\left[\frac{\partial h^{n-1}}{\partial t}\right] + O(\Delta t^2),
\end{aligned} \tag{52}
$$

where we have used the fact that $L_{uh}(u^{n-1}h^{n-1}) = -\frac{\partial h^{n-1}}{\partial t}$. Rearranging, we can write the previous equation as

$$
R^n = R^{n-1} + \Delta t \frac{\partial}{\partial t}\left[\tau_a^{n-1} - C(u^{n-1})^2 + \zeta L_u(u^{n-1}) - \frac{P^*}{2} L_p(h^{n-1})\right] + O(\Delta t^2). \tag{53}
$$

The term inside the brackets is just R^{n-1} so we can write

$$
R^n = R^{n-1} + \Delta t \frac{\partial R^{n-1}}{\partial t} + O(\Delta t^2). \tag{54}
$$

We replace R^n in equation (49) using equation (54) and obtain

$$
\begin{aligned}
\tau_\epsilon =& \Delta t \rho h^{n-1}\frac{\partial u^{n-1}}{\partial t} + \Delta t^2 \rho h^{n-1}\frac{\partial^2 u^{n-1}}{\partial t^2} - \Delta t^2 \rho L_{uh}(u^{n-\frac{1}{2}} h^*)\frac{\partial u^{n-1}}{\partial t} \\
&- \Delta t R^{n-1} - \Delta^2 t \frac{\partial R^{n-1}}{\partial t} + O(\Delta t^3).
\end{aligned} \tag{55}
$$

Using again $L_{uh}(u^{n-\frac{1}{2}}h^*) = L_{uh}(u^{n-1}h^{n-1}) + O(\Delta t)$, we can write

$$\begin{aligned}\tau_\epsilon =&\Delta t\left[\rho h^{n-1}\frac{\partial u^{n-1}}{\partial t} - R^{n-1}\right] + \Delta t^2\left[\rho h^{n-1}\frac{\partial^2 u^{n-1}}{\partial t^2} + \rho\frac{\partial h^{n-1}}{\partial t}\frac{\partial u^{n-1}}{\partial t} - \frac{\partial R^{n-1}}{\partial t}\right]\\ &+ O(\Delta t^3).\end{aligned} \tag{56}$$

Using equation (38), we can eliminate the $O(\Delta t)$ terms. We now use $\frac{\partial}{\partial t}\frac{h\partial u}{\partial t} = h\frac{\partial^2 u}{\partial t^2} + \frac{\partial u}{\partial t}\frac{\partial h}{\partial t}$ to get

$$\tau_\epsilon = \Delta t^2\left[\rho\frac{\partial}{\partial t}h^{n-1}\frac{\partial u^{n-1}}{\partial t} - \rho\frac{\partial u^{n-1}}{\partial t}\frac{\partial h^{n-1}}{\partial t} + \rho\frac{\partial h^{n-1}}{\partial t}\frac{\partial u^{n-1}}{\partial t} - \frac{\partial R^{n-1}}{\partial t}\right] + O(\Delta t^3). \tag{57}$$

$$\tau_\epsilon = \Delta t^2\rho\frac{\partial}{\partial t}\left[h^{n-1}\frac{\partial u^{n-1}}{\partial t} - R^{n-1}\right] + O(\Delta t^3). \tag{58}$$

From equation (38) again, the first term on the right is zero and we find that the truncation error is $O(\Delta t^3)$ which shows that our scheme is second-order accurate in time.

Acknowledgements

We would like to thank William Lipscomb for interesting discussions about the splitting in time instability in sea ice models. We are also grateful to two anonymous reviewers for their helpful comments.

[1] W. D. Hibler, A dynamic thermodynamic sea ice model, J. Phys. Oceanogr. 9 (1979) 815–846.

[2] W. H. Lipscomb, E. C. Hunke, W. Maslowski, J. Jakacki, Ridging, strength, and stability in high-resolution sea ice models, J. Geophys. Res. 112 (2007).

[3] B. Tremblay, L. A. Mysak, Modeling sea ice as a granular material, including the dilatancy effect, J. Phys. Oceanogr. 27 (1997) 2342–2360.

[4] J.-F. Lemieux, B. Tremblay, J. Sedláček, P. Tupper, S. Thomas, D. Huard, J.-P. Auclair, Improving the numerical convergence of viscous-plastic sea ice models with the Jacobian-free Newton Krylov method, J. Comput. Phys. 229 (2010) 2840–2852.

[5] M. Losch, D. Menemenlis, J.-M. Campin, P. Heimbach, C. Hill, On the formulation of sea-ice models. Part 1: Effects of different solver implementations and parameterizations, Ocean Model. 33 (2010) 129–144.

[6] J. Zhang, W. D. Hibler, On an efficient numerical method for modeling sea ice dynamics, J. Geophys. Res. 102 (1997) 8691–8702.

[7] J.-F. Lemieux, B. Tremblay, Numerical convergence of viscous-plastic sea ice models, J. Geophys. Res. 114 (2009) C05009.

[8] E. C. Hunke, Viscous-plastic sea ice dynamics with the EVP model: linearization issues, J. Comput. Phys. 170 (2001) 18–38.

[9] S. Bouillon, T. Fichefet, V. Legat, G. Madec, The elastic-viscous-plastic method revisited, Ocean Model. 71 (2013). 2–12.

[10] J.-F. Lemieux, D. A. Knoll, B. Tremblay, D. M. Holland, M. Losch, A comparison of the Jacobian-free Newton Krylov method and the EVP model for solving the sea ice momentum equation with a viscous-plastic formulation: a serial algorithm study, J. Comput. Phys. 231 (2012) 5926–5944.

[11] M. Losch, A. Fuchs, J.-F. Lemieux, A. Vanselow, A parallel jacobian-free newton-krylov solver for a coupled sea ice-ocean model, J. Comput. Phys. 257 (2014). 901–911.

[12] MITgcm group, MITgcm user manual, online documentation, MIT/EAPS, Technical Report, MIT, 2012. Cambridge, MA 02139, USA. http://mitgcm.org/public/r2_manual/latest/online_documents.

[13] D. R. Durran, P. N. Blossey, Implicit-explicit multistep methods for fast-wave-slow-wave problems, Mon. Wea. Rev. 140 (2012) 1307–1325.

[14] S. Y. Kadioglu, D. A. Knoll, A fully second order implicit/explicit time integration technique for hydrodynamics plus nonlinear heat conduction problems, J. Comput. Phys. 229 (2010) 3237–3249.

[15] S. Y. Kadioglu, D. A. Knoll, R. B. Lowrie, R. M. Rauenzahn, A second order self-consistent imex method for radiation hydrodynamics, J. Comput. Phys. 229 (2010) 8313–8332.

[16] L. Girard, J. Weiss, J. M. Molines, B. Barnier, S. Bouillon, Evaluation of high-resolution sea ice models on the basis of statistical and scaling properties of Arctic sea ice drift and deformation, J. Geophys. Res. 114 (2009).

[17] P. Rampal, J. Weiss, D. Marsan, R. Lindsay, H. Stern, Scaling properties of sea ice deformation from buoy dispersion analysis, J. Geophys. Res. 113 (2008).

[18] H. L. Schreyer, D. L. Sulsky, L. B. Munday, M. D. Coon, R. Kwok, Elastic-decohesive constitutive model for sea ice, J. Geophys. Res. 111 (2006).

[19] L. Girard, S. Bouillon, J. Weiss, D. Amitrano, T. Fichefet, V. Legat, A new modeling framework for sea-ice mechanics based on elasto-brittle rheology, Ann. Glaciol. 52 (2011) 123–132.

[20] K. Wang, C. Wang, Modeling linear kinematic features in pack ice, J. Geophys. Res. 114 (2009) C12011.

[21] M. D. Coon, G. A. Maykut, R. S. Pritchard, D. A. Rothrock, A. S. Thorndike, Modeling the pack ice as an elastic-plastic material, AIDJEX Bulletin 24 (1974) 1–105.

[22] M. McPhee, Ice-ocean momentum transfer for the AIDJEX ice model, AIDJEX Bulletin 29 (1975) 93–111.

[23] M. Kreyscher, M. Harder, P. Lemke, G. M. Flato, Results of the Sea Ice Model Intercomparison Project: Evaluation of sea ice rheology schemes for use in climate simulations, J. Geophys. Res. 105 (2000) 11299–11320.

[24] G. M. Flato, W. D. Hibler, Modeling pack ice as a cavitating fluid, J. Phys. Oceanogr. 22 (1992) 626–651.

[25] J. K. Dukowicz, Comments on the "stability of the viscous-plastic sea ice rheology", J. Phys. Oceanogr. 27 (1997) 480–481.

[26] J.-F. Lemieux, B. Tremblay, S. Thomas, J. Sedláček, L. A. Mysak, Using the preconditioned Generalized Minimum RESidual (GMRES) method to solve the sea-ice momentum equation, J. Geophys. Res. 113 (2008) C10004.

[27] Y. Saad, A flexible inner-outer preconditioned GMRES algorithm, SIAM J. Sci. Comput. 14 (1993) 461–469.

[28] D. A. Knoll, D. E. Keyes, Jacobian-free Newton-Krylov methods: a survey of approaches and applications, J. Comput. Phys. 193 (2004) 357–397.

[29] S. C. Eisenstat, H. F. Walker, Choosing the forcing terms in an inexact Newton method, SIAM J. Sci. Comput. 17 (1996) 16–32.

[30] E. Kalnay, M. Kanamitsu, R. Kistler, W. Collins, D. Deaven, L. Gandin, M. Iredell, S. Saha, G. White, J. Woollen, Y. Zhu, A. Leetmaa, R. Reynolds, M. Chelliah, W. Ebisuzaki, W. Higgins, J. Janowiak, K. C. Mo, C. Ropelewski, J. Wang, R. Jenne, D. Joseph, The NCEP/NCAR 40-year reanalysis project, Bull. Amer. Meteorol. Soc. 77 (1996) 437–471.

[31] W. H. Lipscomb, E. C. Hunke, Modeling sea ice transport using incremental remapping, Mon. Wea. Rev. 132 (2004) 1341–1354.

[32] H.-B. An, Z.-Z. Bai, A globally convergent Newton-GMRES method for large sparse systems of nonlinear equations, Appl. Numer. Math. 57 (2007) 235–252.

[33] M. A. Heroux, R. A. Bartlett, V. E. Howe, R. J. Hoekstra, J. J. Hu, T. G. Kolda, R. B. Lehoucq, K. R. Long, R. P. Pawlowski, E. T. Phipps, A. G. Salinger, H. K. Thornquist, R. S. Tuminaro, J. M. Willenbring, A. Williams, An overview of the Trilinos project, ACM Trans. Math. Soft. 31 (2005) 397–423.

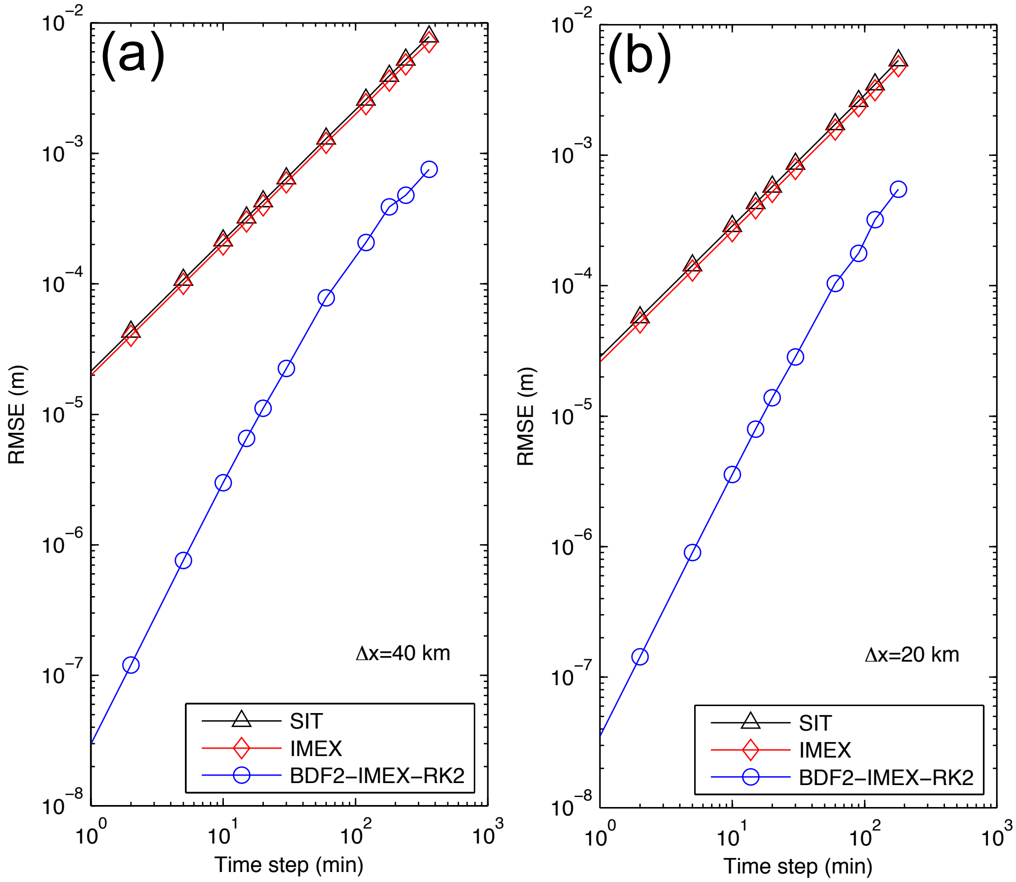

Figure 4: RMSE between an approximate solution and the reference thickness as a function of Δt for spatial resolutions of 40 km (a) and 20 km (b). The black curve with triangles is the SIT method, the red curve with diamonds is the IMEX method while the blue curves with circles is for BDF2-IMEX-RK2.

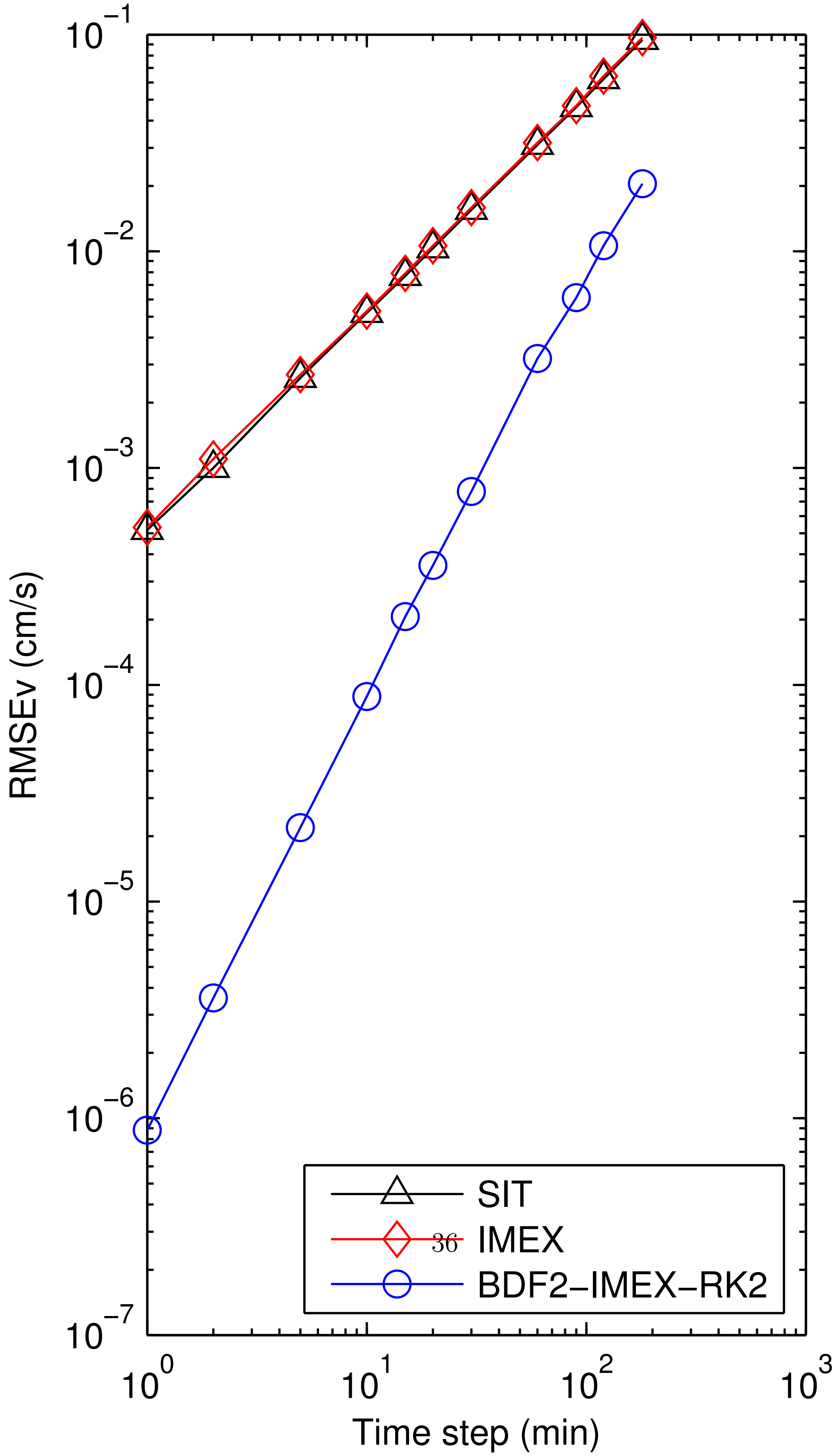

RMSEv (cm/s)
Time step (min)
SIT
IMEX
BDF2−IMEX−RK2
10^−1
10^−2
10^−3
10^−4
10^−5
10^−6
10^−7
10^0
10^1
10^2
10^3

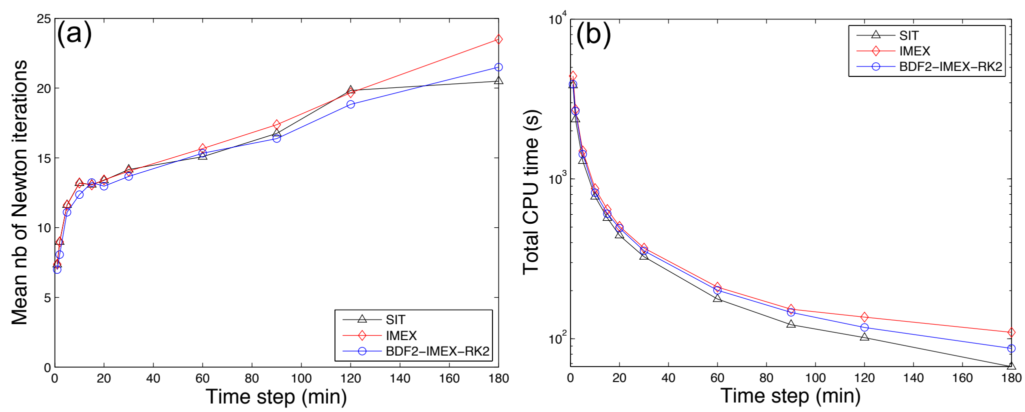

Figure 6: (a) Mean number of Newton iterations per time level as a function of Δt. (b) Total CPU time as a function of Δt. These two quantities were calculated for the last 12 h of the integration. The black curve with triangles is the SIT method, the red curve with diamonds is the IMEX method while the blue curves with circle is for BDF2-IMEX-RK2. The spatial resolution is 20 km.

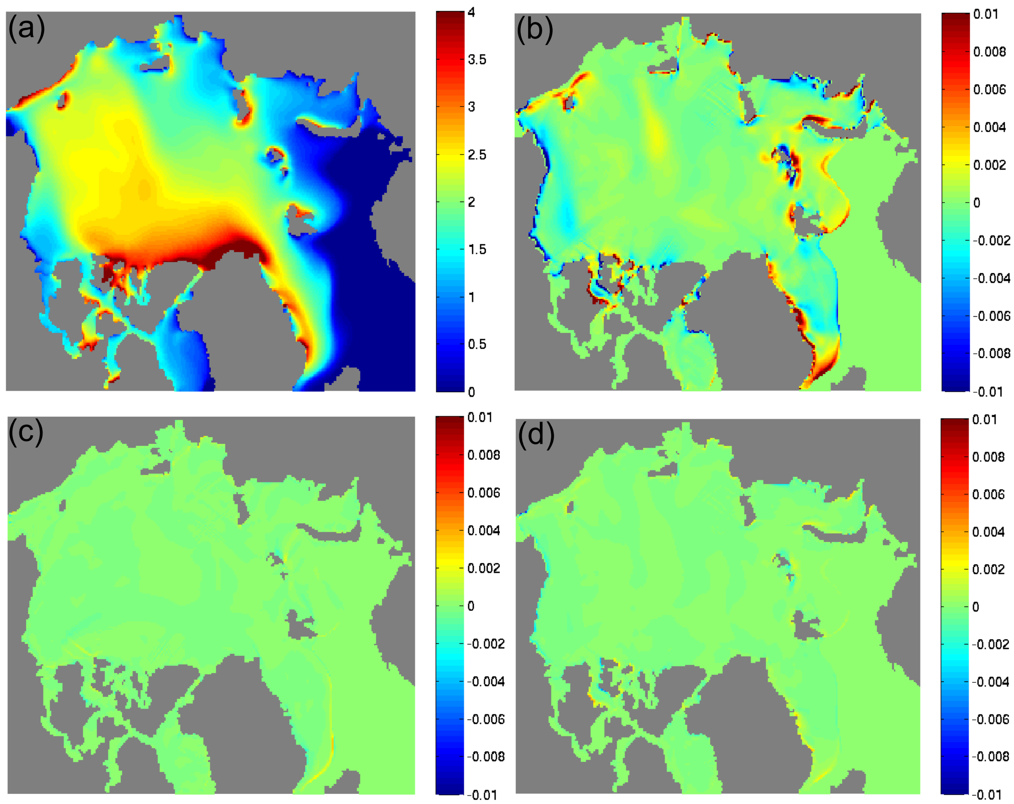

Figure 7: (a) Reference solution thickness field (in m) on 18 January 2002 00Z. This field is capped to 4 m on the figure to see more details. (b) Difference (in m) between the approximate solution obtained with SIT with $\Delta t = 90$ min and the reference solution. (c) Difference (in m) between the approximate solution obtained with BDF2-IMEX-RK2 with $\Delta t = 90$ min and the reference solution. (d) Difference (in m) between the approximate solution obtained with SIT with $\Delta t = 10$ min and the reference solution. The difference fields are capped to ± 0.01 m. Note that the scale is different in (a). The spatial resolution is 20 km.

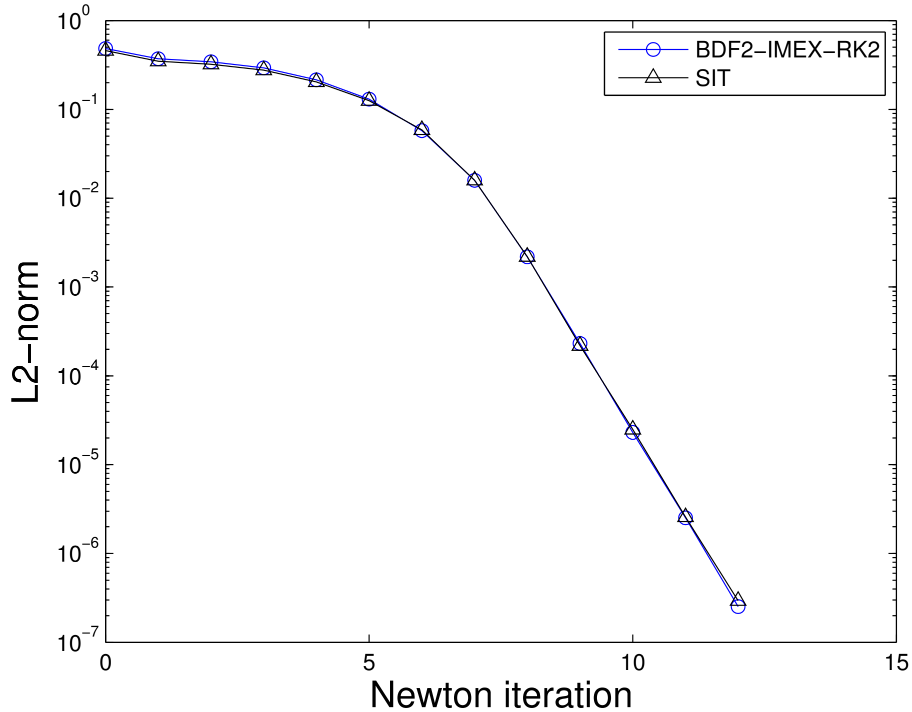

Figure 8: L2-norm on 18 January 2002 00Z as a function of the number of Newton iterations when using the SIT scheme (black curve with triangles) and the BDF2-IMEX-RK2 scheme (blue curve with circles). The time step is 30 min and the spatial resolution is 20 km.